Applied Catalysis B: Environmental 331 (2023) 122688

Contents lists available at ScienceDirect

Applied Catalysis B: Environmental

journal homepage: www.elsevier.com/locate/apcatb

Construction of triazine-heptazine-based carbon nitride heterojunctions boosts the selective photocatalytic C−C bond cleavage of lignin models

Qingqing Zhang [a,1], Yi-Chun Chu [b,1], Zhulan Liu [a], Mei Hong [a], Weiwei Fang [a], Xin-Ping Wu [b,*], Xue-Qing Gong [b], Zupeng Chen [a,*]

[a] *Jiangsu Co-Innovation Center of Efficient Processing and Utilization of Forest Resources, International Innovation Center for Forest Chemicals and Materials, Nanjing Forestry University, Nanjing 210037, China*

[b] *Key Laboratory for Advanced Materials and Joint International Research Laboratory for Precision Chemistry and Molecular Engineering, Feringa Nobel Prize Scientist Joint Research Center, Centre for Computational Chemistry and Research Institute of Industrial Catalysis, School of Chemistry and Molecular Engineering, East China University of Science and Technology, 130 Meilong Road, Shanghai 200237, China*

ARTICLE INFO

Keywords:
Crystalline carbon nitride
Triazine-heptazine heterojunctions
Photocatalysis
C−C bond cleavage
Lignin valorization

ABSTRACT

Photocatalytic lignin depolymerization emerges as a sustainable and cost-competitive strategy to produce low-molecular-weight aromatic chemicals from renewable resources. Significant efforts have been devoted to engineering C−C bond cleavage photocatalysts with diverse compositional and morphologic characteristics in the past decade. We herein present a facile photocatalytic strategy of promoting C−C bond cleavage in lignin models to achieve high-yield aromatic monomers over triazine-heptazine-based carbon nitride heterojunctions, exceeding the triazine- or heptazine-based counterparts. Mechanistic investigations reveal that the photo-excited electron and hole synergistically trigger the C−C bond cleavage. A combination of experimental results and theoretical calculations confirms that the improved photocatalytic performance is primarily attributed to the accelerated charge carriers separation and migration induced by the built-in electric field at the heterojunction interface, and the facilitated C_{β}-radical generation. These findings highlight the effectiveness of interfacial engineering of intramolecular heterostructures towards the rational promotion of photocatalytic cleavage of C−C bond in lignin models.

1. Introduction

The increasing global consumption of nonrenewable fossil fuels has aroused serious concerns about the long-term environmental challenges associated with air pollution and energy shortage, which stimulates the interest in producing high-value liquid fuels and chemicals from renewable carbon resources. Lignin, a key component of lignocellulose (15 −30 wt. %), stores abundant valuable aromatic units *via* labile C−O and recalcitrant C−C bonds [1]. Therefore, the efficient depolymerization of lignin to low-molecular-weight aromatic monomers is an economically viable and fascinating approach for sustainable chemical production from renewable resources and provides an indispensable platform for the promising substitution of petrochemical feedstock by biomass-based chemicals. Unfortunately, lignin has traditionally been regarded as worthless waste in the pulp and paper industry and is directly burned for thermal energy and electricity generation, ignoring its intriguing chemical functionalities [2,3]. In the past few decades, several prominent approaches for the hydrodeoxygenation of lignin into monocyclic aromatics have been reported and made considerable progress, but facing substantial obstacles of serious side-reactions and carbon deposition on the catalyst surface under harsh reaction conditions (*e.g.* high temperature and hydrogen pressure) [4,5].

Currently, photocatalytic lignin depolymerization driven by photogenerated electron-hole coupled mechanism has emerged and come in full flourish rapidly, representing a promising strategy for lignin valorization under mild reaction conditions. This strategy, together with the development of advanced photocatalysts, has undoubtedly led to efficient green chemical production opportunities. Among the tremendous progress in photocatalytic lignin depolymerization, most efforts have been devoted to cleaving the lignin C−O bond over homogeneous or heterogeneous catalysts, but research on the selective breaking of the C−C bond remains sluggish due to its higher bond dissociation energy

* Corresponding authors.
E-mail addresses: xpwu@ecust.edu.cn (X.-P. Wu), czp@njfu.edu.cn (Z. Chen).

[1] These authors contributed equally to this work.

https://doi.org/10.1016/j.apcatb.2023.122688
Received 2 January 2023; Received in revised form 17 February 2023; Accepted 23 March 2023
Available online 24 March 2023
0926-3373/© 2023 Elsevier B.V. All rights reserved.

compared to that of the former (226 −494 *vs.* 209 −348 kJ mol^{-1}) [6,7]. Accordingly, the selective cleavage of the pertinacious C−C bonds should be the major focus but remains challenging for lignin valorization. Previous works have exhibited that β-O-4 or β-1 lignin models can be selectively converted into aromatic monomers by homogeneous or heterogeneous catalysts [8]. In 2020, visible light-driven C−C bond cleavage of β-O-4 lignin model was reported, which depolymerized and transformed the phenolic compounds into high-value products with N-containing groups [9]. Another research describes CuO_x/ceria/anatase nanotube-catalyzed protocol for β-1 lignin model in which surface oxygen vacancies and Ce^{3+} ions were demonstrated to be the reactive species to initiate the C−C bond cleavage [10]. Moreover, iridium and vanadium-based catalysts, as well as ionic liquid (Scheme 1a), have been proven to effectively improve the selectivity toward C−C bond cleavage in β-O-4 or β-1 lignin models [11–14], boosting the production of low-molecular-weight aromatic monomers. Despite impressive progress made in the desired C−C bond cleavage, the homogenous nature of the metal complex catalysts suffers from the problems of separation and reusability, therefore tremendously limiting the practical large-scale applications and leaving the scope for further development in a sustainable manner. Within this context, developing metal-free heterogeneous photocatalysts offers many advantages, including the considerably lower price, high stability, and efficient recycling.

The metal-free polymeric carbon nitrides (CN), owing to their unique features such as appealing π-conjugated electronic structures, high stability, earth-abundance, and low toxicity, have received intensive attention from different fields of water splitting [15,16], CO_2 reduction [17], environmental remediation [18,19] and C−C bond cleavage (Scheme 1b) [20]. However, the photocatalytic activities of the pristine bulk CN are limited by the rapid charge carrier recombination, limited surface area, and low crystallinity. Strategies such as elemental doping [21,22], heterojunction construction [23,24], co-catalyst deposition [25], and morphology modulation [26] have been employed to improve the photocatalytic performance over the past decades. Among these strategies, building an electric field by constructing heterojunctions is an outstanding approach to facilely enable the effective separation of photo-excited electron-hole pairs and subsequent transfer across the interface in the junction region [27]. Sels and Wang described a redox strategy for cleaving the C−C bond of lignin β-1 models to benzaldehyde with Z-scheme Ag_3PO_4-CN nanocomposites as the effective heterogeneous photocatalyst [28].

The structural designability and promising catalytic activity of carbon nitrides make them good candidates as heterogeneous photocatalysts for the successful cleavage of the C−C bonds in lignin models. Encouraged by the inherent advantages, we herein report a practical, efficient, and eco-friendly strategy for aromatic monomers formation in excellent yields through triazine-heptazine donor-acceptor (D-A) heterojunctions-catalyzed C−C bonds cleavage of lignin β-O-4 models under blue LED irradiation and O_2 atmosphere (Scheme 1c). It is remarkable that the carbon nitride heterojunctions with a strong interfacial electric field formed in an *in-situ* manner endow intimate contact and prompt charge carrier separation. Mechanism investigations verify the radical-mediated photocatalytic redox-neutral mechanism driven by photo-excited electron-hole pairs. Density functional theory (DFT) calculations demonstrate that the triazine-heptazine heterojunctions significantly lower the dehydrogenation energy barrier for the C_β-radical generation, which favors C−C bond cleavage. Therefore, the present photocatalytic method not only enriches existing protocols for the valorization of lignin models but also advances a significant step toward the application of renewable biomass.

2. Experimental

2.1. Materials

Urea, potassium chloride (KCl), sodium chloride (NaCl), lithium chloride (LiCl), and 2-phenoxy-1-phenylethanol were purchased from Aladdin (Shanghai, China). Acetonitrile (MeCN) was purchased from Sinopharm Chemical Reagent Co., Ltd. (Shanghai, China). All chemicals

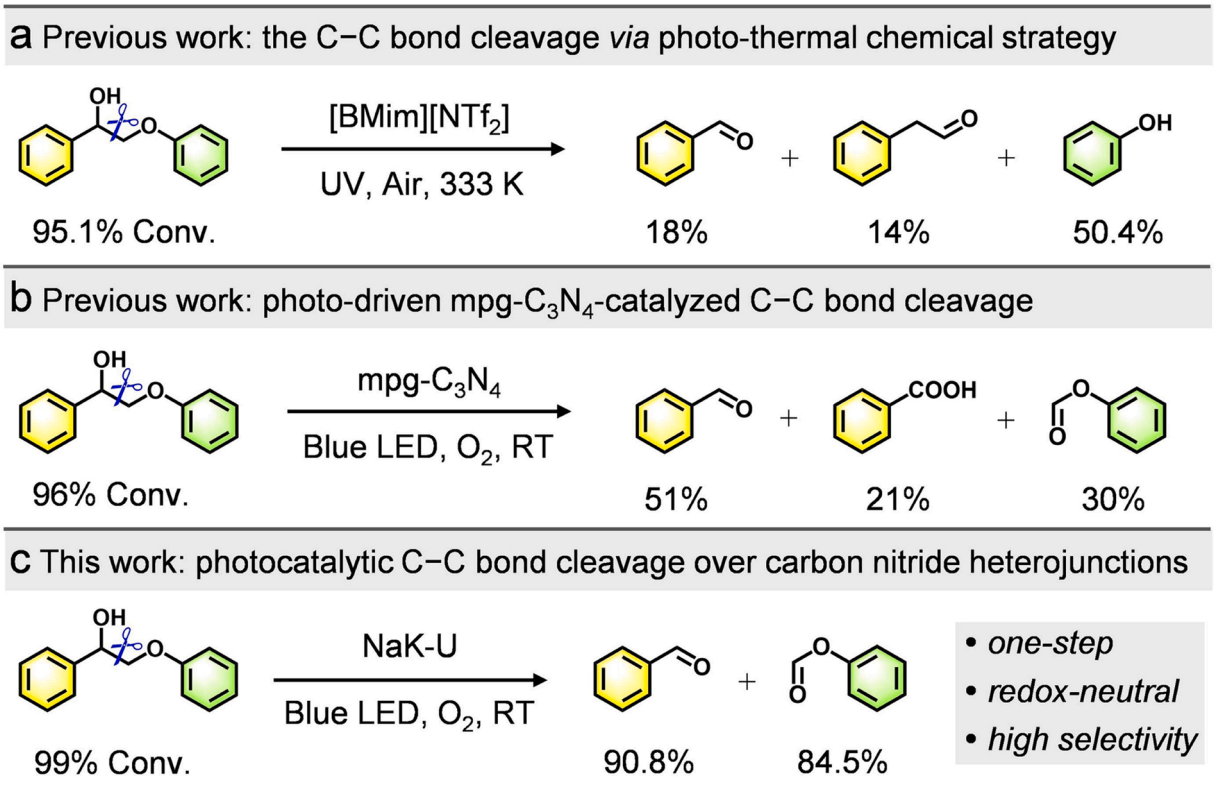

Scheme 1. Methods for the C−C bond cleavage of β-O-4 lignin model.

are of analytic grade and were used as received without further purification.

2.2. Catalyst preparation

Triazine-heptazine-based carbon nitride heterojunctions were synthesized by a typical molten salt-assisted copolymerization process following a previously reported method [29]. In a typical procedure, the starting nitrogen-rich precursors (urea, melamine, or 5-aminotetrazole, 20 g) were thoroughly grounded with KCl (9 g) and NaCl (11 g) in a crucible. Subsequently, the mixture was calcined at 823 K for 4 h in a muffle furnace with a heating rate of 2.3 K min^{-1} under an N_2 atmosphere. After being fully washed with abundant deionized water, the final pale-yellow solid was collected after drying at 353 K in an electric oven. The carbon nitride prepared from urea, melamine, or 5-aminotetrazole in NaCl/KCl binary eutectic salts was labeled as NaK-U, NaK-M, or NaK-A, respectively. For comparison, Na-U, K-U, Li-U, and LiK-U were prepared from urea with a similar method in the presence of single salt (NaCl, KCl, or LiCl) or LiCl/KCl molten salts.

2.3. Catalyst characterization

Power X-ray diffraction (XRD) data were collected using a Rigaku X-ray diffractometer (ULTIMA IV) with Cu Kα radiation ($\lambda = 1.54056$ Å) at an accelerating voltage of 40 kV. The morphologies were observed by scanning electron microscope (SEM) (Regulus-8100, Hitachi) and high-resolution transmission electron microscopy (HRTEM) (JEM-2100 UHR, Jeol). N_2 physisorption isotherms were recorded to determine surface areas and pore volumes using a Micromeritics ASAP2020 HD88 setup operating at 77 K. Elemental analysis was performed on a Perkin-Elmer PE 2400 II elemental analyzer. Fourier transformed infrared (FTIR) spectra were recorded on a Bruker VERTEX 80 V instrument. X-ray photoelectron spectroscopy (XPS) was carried out on a Shimadzu AXIS Ultra DLD, equipped with a monochromatic Al Kα source (150 W). The UV-Vis diffuse reflectance spectra (UV-Vis/DRS) were collected on a UV-Vis spectrophotometer (UV-3600, Shimadzu). Solid-state ^{13}C cross-polarization magic-angle-spinning nuclear magnetic resonance (CP-MAS NMR) was recorded on a Bruker AVANCE AV-600 spectrometer. The photoluminescence (PL) spectra and time-resolved photoluminescence decay (TRPD) spectra were measured on Hitachi FL4700, and Edinburgh FLS980 fluorescence spectrophotometers, respectively. 2,2,6,6-Tetramethyl-1-piperinedinyloxy (TEMPO)-tapping electron spin resonance (ESR) spectra were performed on a Bruker EMXplus spectrometer under visible-light irradiation. The transient photocurrent response, electrochemical impedance spectroscopy (EIS) Nyquist plots, and Mott-Schottky plots of the prepared carbon nitrides were performed in a three-electrode system made of quartz with an electrochemical workstation (CHI660E, Chenhua Instruments Co., China). Specifically, fluorine-doped tin oxide (FTO) coated with the carbon nitride film (diameter of 0.6 cm) served as the working electrode, while Pt wire and Ag/AgCl electrode were used as the counter and reference electrodes, respectively. A 300 W Xenon lamp and 0.2 mol L^{-1} Na_2SO_4 aqueous solution were applied as light source and electrolyte, respectively. Surface photovoltage (SPV) spectroscopy was recorded on a steady-state surface photovoltage spectrometer (PL-SPV/IPCE1000 Beijing Perfectlight Technology Co, Ltd).

2.4. Photocatalytic C−C bond cleavage of lignin models

The photocatalytic C−C bond cleavage was carried out in a quartz tube *via* bottom irradiation with a 40 W blue LED light (Kessil) under $\lambda = 427$ nm using a parallel photocatalytic reactor (SCI-PCRS-3–427-H-ET, Anhui Chem-n Instrument Co., Ltd.). Typically, lignin model compounds (0.05 mmol), acetonitrile (1 mL), and catalyst (10 mg) were added into a quartz tube. Prior to the reaction, the reactor was evacuated and purged with N_2, O_2, or air for 5 min. The temperature of the reaction raised to 35 ℃ spontaneously during the reaction. *CAUTION: The eyes need protection by wearing goggles to prevent injury from 427 nm light.* After the reaction, the mixture was filtered through a 0.22 μm Nylon filter and then analyzed by gas chromatography (GC) using *n*-dodecane as the internal standard.

2.5. Details of density functional theory (DFT) calculations

Spin-polarized DFT calculations were carried out by using the *Vienna ab initio simulation package* (*VASP*) [30,31]. The Perdew−Burke−Ernzerhof (PBE) [32] exchange-correlation functional under the generalized gradient approximation (GGA) with the D3 dispersion correction of Grimme [33] was used. The valence-core interactions were described by the projector augmented-wave (PAW) [34] method. The plane-wave cutoff energy was set at 400 eV, and a $3 \times 3 \times 1$ *k*-point mesh was used for the Brillouin-zone integrations. Geometry optimizations were finished until the Hellman-Feynman force on each relaxed ion was less than 0.05 eV/Å. Frequency analyses ensure that each transition state structure has only one imaginary frequency.

The single-layer triazine and heptazine CN were extracted from the corresponding bulk structures and extended at a 4×4 and 3×3 surface cell, respectively. The calculated lattice parameters of single-layer triazine and heptazine CN are a = b = 18.90 Å and a = b = 20.90 Å, respectively (Fig. S1a,b). The single-layer triazine-heptazine-CN model composed of alternating links of triazine (C_3N_3) and heptazine (C_6N_7) with lattice parameters of a = 22.00 Å and b = 18.30 Å was also constructed (Fig. S1c). For the three kinds of CN surfaces, a vacuum layer of 25 Å which is perpendicular to the surface was included to avoid interactions between the slabs.

3. Results and discussion

3.1. Structure and morphology characterizations

Carbon nitride materials (NaK-*X*, *X* refers to the precursors, *i.e.*, U (urea), M (melamine), or A (5-aminotetrazole)) were synthesized *via* one-pot NaCl/KCl eutectic mixture-induced thermal polymerization by employing different precursors with distinct melting points (urea: 405 K; melamine: 627 K; 5-aminotetrazole: 479 K) (Fig. 1a). The binary molten salts of NaCl/KCl not only acted as the solvent to provide a semi-liquid environment in the high-temperature polymerization process but also endowed the cations (K^+, Na^+) with a structure-directing influence on the layer stacking. The introduction of eutectic molten salt media and the screen of the nitrogen-rich precursors could improve the structural order and crystallinity, and thus regulate the microscopic structure of the carbon nitrides. The morphological characteristics of the as-prepared crystalline carbon nitride (CCN) samples were investigated by scanning electron microscope (SEM) and transmission electron microscope (TEM). NaK-U (Fig. 1b, e) and NaK-M (Fig. 1c, f) exhibited the stacking nanostructures with nanoparticles and flakes, respectively. In contrast, NaK-A presented a bulk structure (Fig. 1d, g), indicating that the morphologies of NaK-*X* samples highly depended on the type of starting precursors. Among the obtained CCN, NaK-U displayed small nanoparticles with an irregular distribution, thus offering a significantly higher number of active sites than NaK-M and NaK-A with larger aspect ratios. For comparison, LiCl/KCl-induced LiK-U displayed a petal-like structure, while the single, non-eutectic metal salt-induced Na-U, K-U, and Li-U exhibited irregular rod-like or bulky structures (Fig. S2). Collating these results enabled a deduction that the nanoparticle or nanosheet features of binary eutectic salts-induced NaK-U and LiK-U was probably ascribed to the confinement effect of binary eutectic salts and the interaction of alkali metal cations between the heterocyclic units, promoting the effective exfoliation of bulk carbon nitride [35,36]. High-resolution (HR) TEM was conducted to get more structural insight into the NaK-*X* samples, validating the high local order and crystallinity of the obtained CCN from the NaCl/KCl eutectic mixture (Fig. 1h-j).

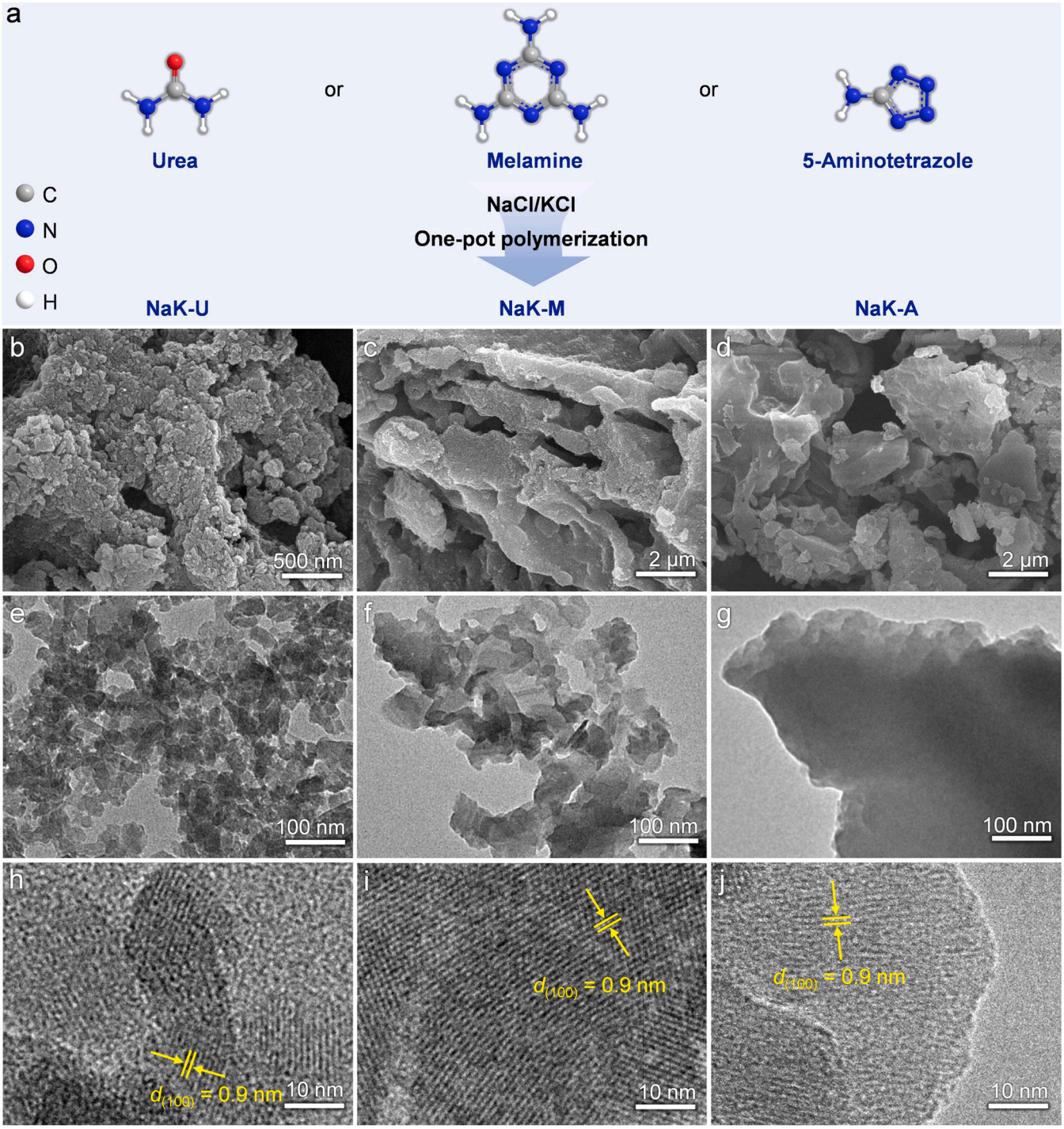

Fig. 1. Synthetic route for the construction of NaK-*X* (a). SEM (b-d), TEM (e-g) and HRTEM (h-j) images of NaK-U (b, e, h), NaK-M (c, f, i), and NaK-A (d, g, j).

Clear lattice fringes were observed in the cases of NaK-U, NaK-M, and NaK-A (0.9 nm), which could be assigned to the (100) planes with the same packing distance of the in-plane triazine/heptazine units [37,38].

The significantly enhanced surface area of NaK-U (82.6 $m^2\ g^{-1}$) with respect to NaK-M (6.7 $m^2\ g^{-1}$), NaK-A (5.0 $m^2\ g^{-1}$), and other single metal salt-induced CCN, was revealed by N_2 adsorption-desorption isotherms (Table S1), reflecting in higher uptakes over the whole range of relative pressure and associated pore volume (Fig. S3). This was resulted from the lowest melting point of urea as well as the solvent effect of molten salt mixture NaCl/KCl. On the one hand, urea with a lower melting point may decompose into large amounts of NH_3 and CO_2, serving as the supplementary nitrogen-source and bubble-generating template respectively. On the other hand, the melting point of the molten salts NaCl/KCl (923 K) is lower than that of NaCl (1073 K) and KCl (1043 K) but higher than the polymerization temperature (823 K), which may provide a "semi-liquid-solution", serving as the (micro) structure-directing agent to drive high local order and crystallinity. Furthermore, the elemental analysis revealed that the C/N atomic ratios of NaK-*X* (0.69) and other CCN samples (0.69 −0.72) were higher than that of the typical melon-type bulk carbon nitrides (*e.g.*, BCN, C/N = 0.67), indicating the fewer terminal $-NH_2$ groups and higher crystallinity in the molten salt-induced carbon nitrides.

Powder X-ray diffraction (XRD) confirmed the distinct crystalline structures of the resulting CCN samples. As shown in Fig. 2a, NaK-M and NaK-A featured two typical diffraction peaks of the heptazine phase, corresponding to the in-plane periodic arrangement (100) and the π-π interlayer stacking (002) of the heptazine units, respectively. However, significant phase changes were observed for LiK-U, which showed many well-resolved reflections at 11.8, 20.9, 24.4, 26.5, 29.2, and 32.3° (Fig. S4a), which could be ascribed to the (100), (110), (200), (002), (102) and (210) planes of the triazine-based carbon nitride (T-CN) [39, 40]. Comparatively, in the pattern of NaK-U, it was very interesting to observe a superimposition of characteristic peaks from both the heptazine phase and triazine phase, suggesting the *in-situ* construction of triazine-heptazine D-A heterojunctions [41]. The evident change in the crystalline structure was tentatively ascribed to different condensation degrees and polymerization kinetics of starting monomers in NaCl/KCl molten salts. Additionally, the NaCl/KCl molten salts may contribute to the partial "dissolution" of urea-derived melon, achieving the partial structural transformation from heptazine to triazine to form a well-designed D-A heterojunctions structure [42]. For all NaK-*X* samples, the low diffraction degree of (100) peaks located at 7.8° was in agreement with the large fringe separation ($d_{(100)} = 0.9$ nm) in the HRTEM images (Fig. 1h-j), resulting from the incorporation of Na^+ and K^+ cations between the triazine/heptazine units [35,43]. The second diffraction peak of NaK-M exhibited a noticeable right-shift from 27.4° to 28.1° with a narrowed half peak width compared to NaK-A, evidencing the narrower interlayer spacing narrowing from 0.325 to 0.317 nm [44,45]. It was noticeable that two (002) peaks located at 27.4 and 28.0° were found in NaK-U, indicating the formation of D-A heterojunctions resulted in changes in the interplanar stacking distance. In addition, the Li-U, K-U, and Na-U synthesized with single metal salts possessed different diffraction peaks at $2\theta = 26.7$, 28.3, and 27.4°, corresponding to the heptazine units stacking along (002) direction (Fig. S4a).

Analysis by Fourier transform infrared (FTIR) spectra of the synthesized samples confirmed the existence of condensed aromatic CN heterocycles and similar functional groups (Fig. 2b and S4b). The evident vibration peaks in the ranges 700 – 850 cm^{-1} and multiple broad peaks located at 1200 – 1600 cm^{-1} were assigned to out-of-plane bending vibrations and characteristic stretching vibrations of aromatic CN-heterocycles, respectively. The broad absorption bands at 3300 – 3600 cm^{-1} were attributed to the stretching vibrations of the terminal $-NH_x$ groups on the CN heterocyclic ring [46]. Furthermore, compared to NaK-A, NaK-U and NaK-M showed weakened vibration intensities of terminal/bridging unreacted N–H, illustrating the higher degree of polymerization and crystallinity of NaK-U and NaK-M than NaK-A, which was in agreement with the result of XRD pattern. Noted that the characteristic peaks located at 993 and 1151 cm^{-1} correspond to the symmetric and asymmetric variations of $Na/K-NC_2$ units [47]. The distinct peaks located at 2180 and 2145 cm^{-1} indicated the presence of terminal cyano groups (−C≡N), probably stemming from the decomposition or incomplete polymerization of triazine/heptazine units [48].

Further insights into the surface structure of the NaK-*X* samples were obtained by X-ray photoelectron spectroscopy (XPS) analysis. The survey XPS spectra evidenced the presence of C, N, O, Na, and K in all NaK-*X* samples (Fig. S4c). The fitted C 1 s XPS spectra presented three main contributions (Fig. 2c): the main peak at 288.3 eV was ascribed to sp^2-hybridized carbon, which was derived from the N – C=N in the framework of the CN heterocyclic ring; while the two small peaks centering at 284.8 and 286.4 eV were assigned to carbon atoms from the adventitious carbon, and $C-NH_x$, or −C≡N groups on the edges of the CN heterocyclic ring [49]. In addition, two K 2p peaks located at 296 and 293.2 eV with a doublet separation energy of 2.8 eV indicated the oxidation states of K^+ ions in NaK-*X* [50]. Comparatively,

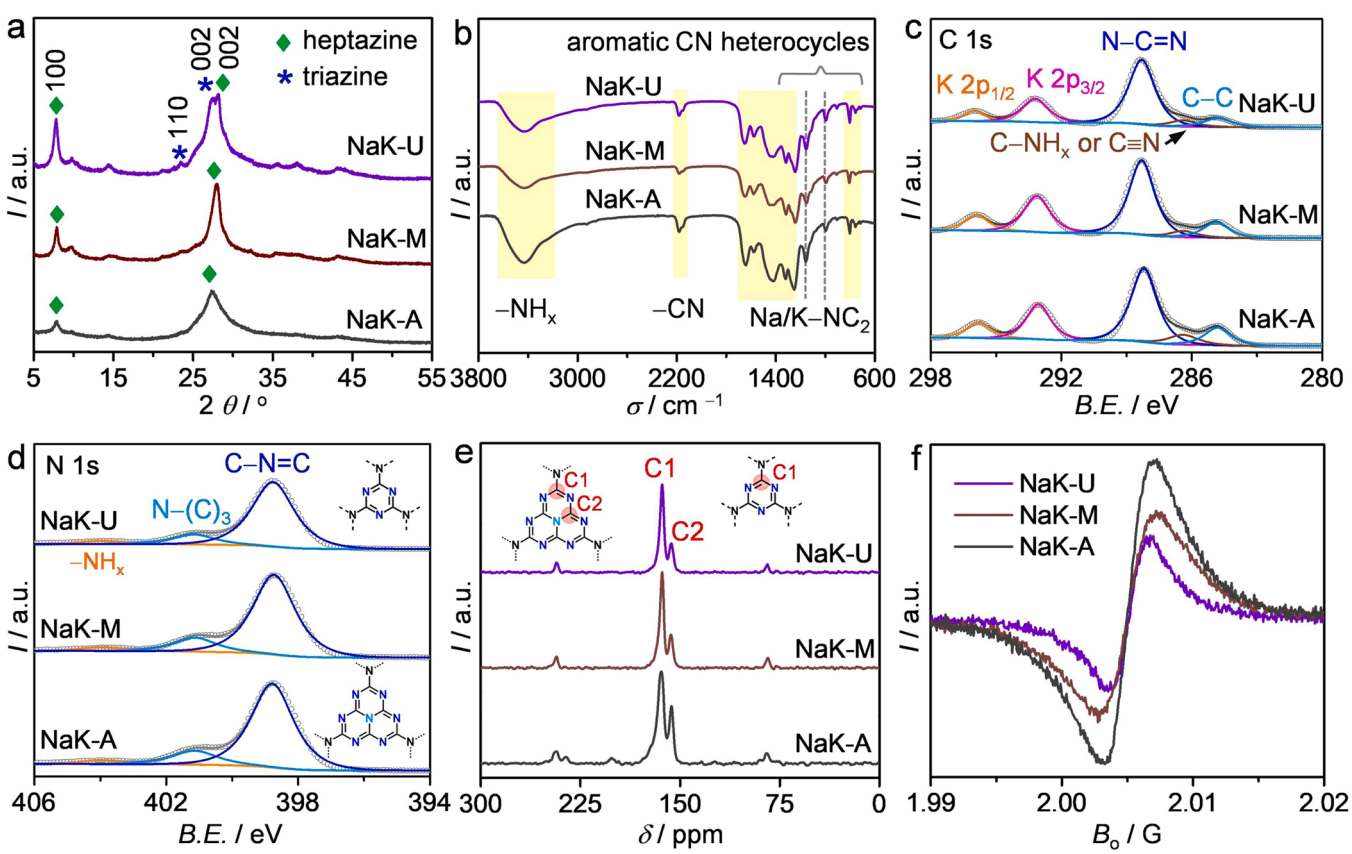

Fig. 2. XRD patterns (a), FTIR spectra (b), high-resolution C 1 s (c), N 1 s (d) XPS spectra, ^{13}C CP-MAS NMR spectra (e) and ESR spectra (f) of NaK-U, NaK-M and NaK-A.

high-resolution N 1 s XPS spectra also showed three binding energy peaks (Fig. 2d). The strongest peaks at 398.7 eV were assigned to the sp^2-hybridized N atoms in the CN heterocyclic ring (C−N = C). The secondary peaks at 401.1 eV originated from the tertiary N atoms from N − $(C)_3$ groups in the heptazine units according to the conjugated carbon nitride structures inserted in Fig. 2d [51]. While the smallest peaks at 404 eV corresponded to the surface primary/secondary amine groups ($-NH_x$) [52]. Note that the peak-area ratio between C−N = C and N − $(C)_3$ of NaK-U (6.5) was significantly higher than that of NaK-M (5.7) and NaK-A (5.7), indicating the partial structure transformation from the heptazine rings to triazine rings [42], which strongly demonstrate that the existence of isotype triazine-heptazine heterojunctions in NaK-U [42].

The obtained NaK-*X* samples were further structurally characterized by solid-state ^{13}C nuclear magnetic resonance (NMR). All samples presented two distinct peaks situated at 163.5 and 156.8 ppm (Fig. 2e), which could be assigned to C1 atoms ($CN_2(NH_x)$) of triazine/heptazine-based units and C2 atoms (CN_3) of heptazine-based units, respectively [45,53]. It was noticed that the peak intensity of C2 declined markedly in comparison with C1, clearly suggesting the emergence of nitrogen vacancies in the carbon nitride skeleton [16]. Moreover, the C1/C2 peak-area ratios increased from 2.6 (NaK-A, NaK-M) to 2.9 (NaK-U),

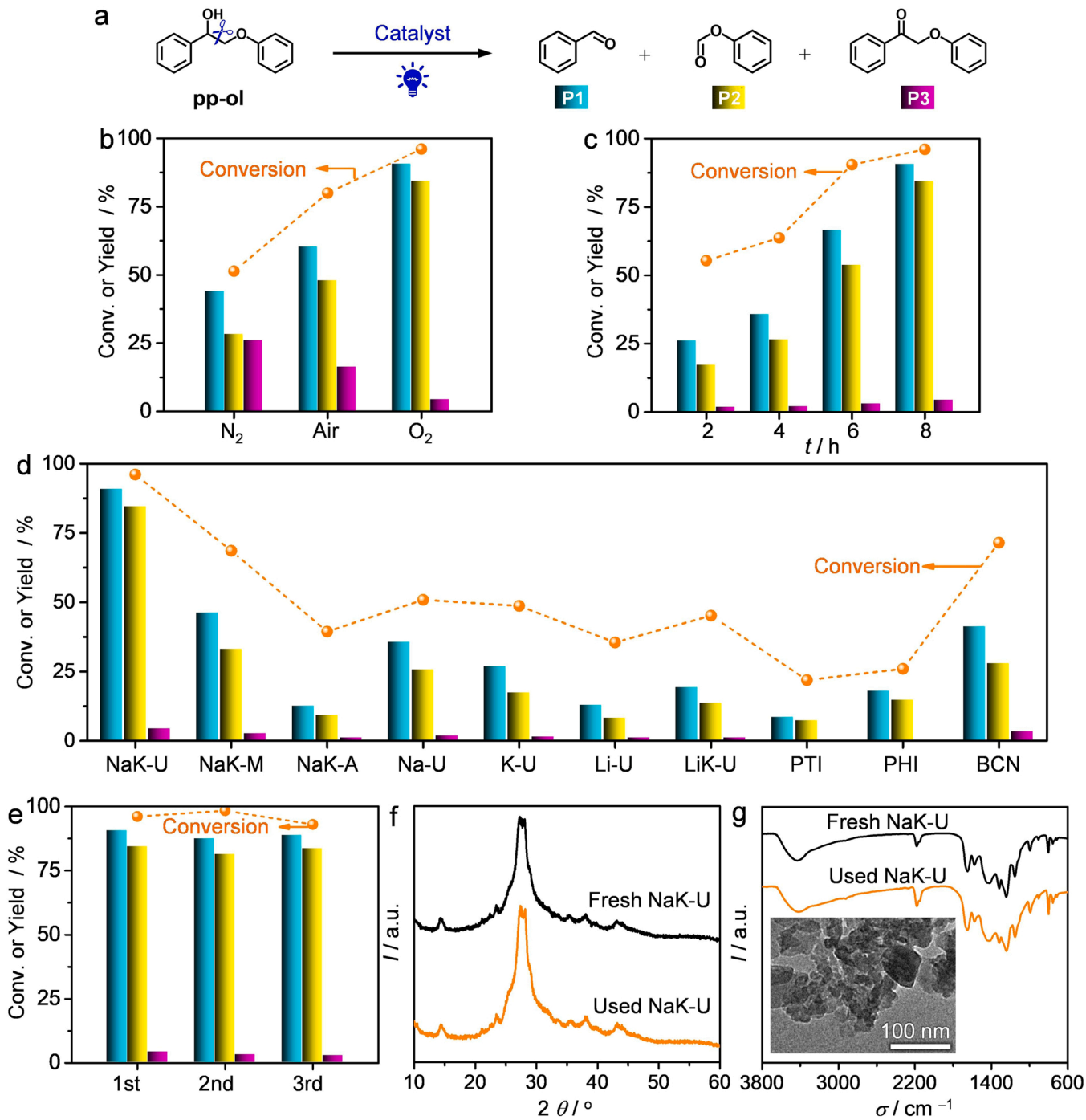

Fig. 3. Photocatalytic depolymerization of pp-ol (a). Atmosphere (b), time (c) and catalyst scanning (d) in MeCN for photocatalytic depolymerization of pp-ol. Recycling stability evaluation of NaK-U (e). XRD patterns (f) and FTIR spectra (g) and TEM image (inset) of the used NaK-U. Reaction conditions: 0.05 mmol pp-ol, 10 mg NaK-U, 1 mL MeCN, 8 h (a), O_2 (b), 10 mg catalyst (d).

suggesting more C1 atoms in NaK-U derived from triazine-based units and further proving the successful formation of isotype triazine-heptazine heterojunctions in NaK-U, consistent with the results of XRD and N 1 s XPS.

To get more insightful information about the electronic structure of NaK-*X*, the electron spin resonance (ESR) spectra were recorded at room temperature. As shown in Fig. 2f, three samples presented essentially the same paramagnetic absorption signal at $g = 2.005$, indicating the same type of unpaired electrons on π-conjugated aromatic heterocycles [54, 55]. However, a substantial decline of the ESR signals was observed in the order of NaK-A > NaK-M > NaK-U, suggesting a decreased unpaired electrons density owing to the lower density of structural defects and higher crystallinity, which further clarified the key point of increasing extended π-conjugation and hence an encouraging separation and transport of charge carriers at the contact interfaces of triazine-heptazine-based heterojunctions [56].

3.2. Photocatalytic C−C bond cleavage

The photocatalytic reactions were performed using a representative and widely used lignin β-O-4 model compound, 2-phenoxy-1-phenylethanone (pp-ol), as the starting substrate (Fig. 3a). The effect of the reaction atmosphere was first screened to enhance the conversion of the pp-ol over NaK-U catalyst in MeCN, showing distinct product distribution in the present photocatalytic system. As shown in Fig. 3b, the O_2 atmosphere presented a significantly improved pp-ol conversion (96.1 %), which was 1.2 times that of air (80 %) and about 2 times that of N_2 (51.4 %). To be more specific, the yields toward C_α−C_β bond cleavage products benzaldehyde (P1) and phenyl formate (P2) in N_2 were determined to be 44.0 % and 28.2 %, respectively, and the yield toward C_α−OH oxidative product 2-hydroxy-1-phenylethanone (P3, pp-one) was found to be 25.9 %. Interestingly, when the performance was examined in the air, the yields of P1 and P2 could be further boosted to 60.3 % and 47.9 %, respectively, while the yield of P3 was determined as 16.2 %. What's more, in contrast to the dissatisfactory activity in N_2 and air, NaK-U exhibited significantly enhanced yields of P1 and P2 in O_2. Simultaneously, the formation of oxidative product (pp-one) was remarkably inhibited with a low yield of 4.2 %. Therefore, the excellent photocatalytic performance in O_2 unambiguously demonstrated that the photo-driven C−C bond cleavage of pp-ol was an O_2-engaged reaction. Furthermore, the yield–irradiation time relationships of photocatalytically produced P1 and P2 with NaK-U as the photocatalyst using O_2 as the feed gas was recorded in Fig. 3c, showing that the produced P1 and P2 amount increased linearly with the irradiation time and the highest aromatic monomers yields were identified as 90.8 % (P1) and 84.5 % (P2) under O_2 atmosphere for 8 h. In addition, the outstanding selectivity in the NaK-U-photocatalyzed C−C bond cleavage of pp-ol was further demonstrated by the GC-MS analysis (Fig. S5).

Subsequently, photocatalytic activities of various carbon nitrides were then evaluated in the production of aromatic monomers from the C−C cleavage of pp-ol under the optimized conditions (O_2 as the feed gas and 8 h of irradiation) (Fig. 3d). Compared to NaK-U, other as-prepared CCN catalysts (*i.e.*, NaK-M, NaK-A, Na-U, K-U, Li-U, and LiK-U) presented lower activity for pp-ol depolymerization, with the conversions decreased to 35.5 − 68.6 % and the yields towards P1 and P2 reduced to 12.4 − 46.1 % and 8.1 − 33 %, respectively. Additionally, the widely reported highly crystalline poly(triazine imide) (PTI) and poly(heptazine imide) (PHI) exhibited relatively low conversion and yields of cleavage products. Taking the typical melon-type bulk carbon nitrides (*i.e.*, BCN) as the photocatalyst, the pp-ol was transformed into aromatic monomers (P1 and P2) with unsatisfying yields, demonstrating the inferior C−C cleavage selectivity. These results highlight the critical role of the construction of triazine-heptazine D-A type heterojunctions, instead of the single triazine or heptazine units. Furthermore, the photocatalytic stability for NaK-U was investigated by performing three consecutive catalytic runs under the optimized reaction conditions, showing neglectable variations of the total conversion of pp-ol, and the monomer yields towards P1, P2, and P3 (Fig. 3e). Analysis of the spent catalyst by XRD, FT-IR, and TEM, highlighted the identical structure and morphology (Fig. 3f, g).

To explore the potential regarding the availability of NaK-U, the typical β-O-4 substrates containing different substituted functional groups (*e.g.*, −OMe, and C_γ−OH groups) and β-1 substrate were explored. Given the results of catalytic funneling in Table S2, all β-O-4 substrates could be successfully converted into aromatic monomers, showing good substrate scope and product yields. Nonetheless, yields of the aromatic monomers with methoxy groups were low due to the over-oxidation or polymerization of cleaved aromatic compounds or intermediates under light irradiation. The generation of phenolic compounds may be caused by the decomposition of phenyl formate. While, the lignin β-1 model (1,2-diphenylethanol) was converted into the corresponding oxidation product (1,2-diphenylethanone), with an isolated yield of 96 %. These results indicate the applicability of the NaK-U is almost exclusively confined to the β-O-4 substrates, which is of high significance since this type of linkage is known as the most common lignin-derived building block constituting 43 − 62 % of native lignin linkages.

3.3. Photoelectrochemical properties

To obtain insights into the optical and electrical properties of NaK-*X*, various photo- and photoelectrochemical techniques were employed. According to the UV-Vis diffuse reflectance spectra (DRS) (Fig. 4a), an intrinsic optical absorption band of carbon nitrides in the wavelength range of 300–480 nm was found, which was caused by the π-π * electronic transitions in the π-conjugated CN heterocycles. To be more specific, NaK-U exhibited enhanced light absorbance in the range of 300 − 430 nm compared with NaK-A and NaK-M, suggesting the higher stabilization of photo-generated electron-hole pairs presumably in consequence of the co-existence of triazine- and heptazine-based structure [41,42]. In addition, the UV-Vis DRS of NaK-A showed a new absorption band at 450–620 nm, which was assigned to the n-π * electron transition, further confirming the presence of plenty of unpaired electrons in the edge N atoms of the CN heterocyclic ring, consistent with the ESR results [22,57]. In addition, the direct band gaps (E_g) estimated from the corresponding Tauc plots were calculated to be 2.54, 2.50, and 2.35 eV for NaK-U, NaK-M, and NaK-A, respectively. Meanwhile, the UV-Vis DRS and band gaps of Na-U, K-U, Li-U, and LiK-U were displayed in Fig. S4d. To provide detailed band structure alignments regarding the valance band (VB) and conduction bands (CB) of the NaK-*X* samples, the Mott-Schottky plots and VB-XPS spectra were further carried out. The Mott-Schottky plots in Fig. S6a–c exhibited positive slops, demonstrating the *n*-type semiconductors for NaK-*X* samples [58]. Moreover, it was generally accepted that the tangent intersections of Mott-Schottky curves at different frequencies (1.3, 1.5, and 1.8 kHz) represented the Fermi level positions (E_F). Besides, the energy difference (δ_p) from the VB to the Fermi level can be extrapolated from the corresponding VB-XPS spectra, as displayed in Fig. 4b. Based on the equation of $E_{VB} = \delta_p + E_F$, VB edges of NaK-*X* samples were determined [59]. Apparently, the CB values of NaK-*X* were determined to be − 0.91, − 0.81, and − 0.60 eV (*vs.* reversible hydrogen electrode) in terms of $E_{CB} = E_g - E_{VB}$, respectively. Knowing the bandgap values and the VB, as well as the CB position, the corresponding band structures of NaK-X samples, were schematically depicted in Fig. S6d. Compared to pristine CN (2.70 eV), the bandgaps of NaK-*X* were narrowed to 2.54 (NaK-U), 2.50 (NaK-M) and 2.35 eV (NaK-A) as a result of distinct down-shifted VB and CB edges. The above results illustrate that the formation of T/H-CN heterojunction increases the CB position, endowing the stronger reduction capacity of NaK-U which is tremendously favorable to the optimized redox ability of the NaK-U for C−C bond cleavage.

The emission properties and the fluorescence lifetimes of the charge

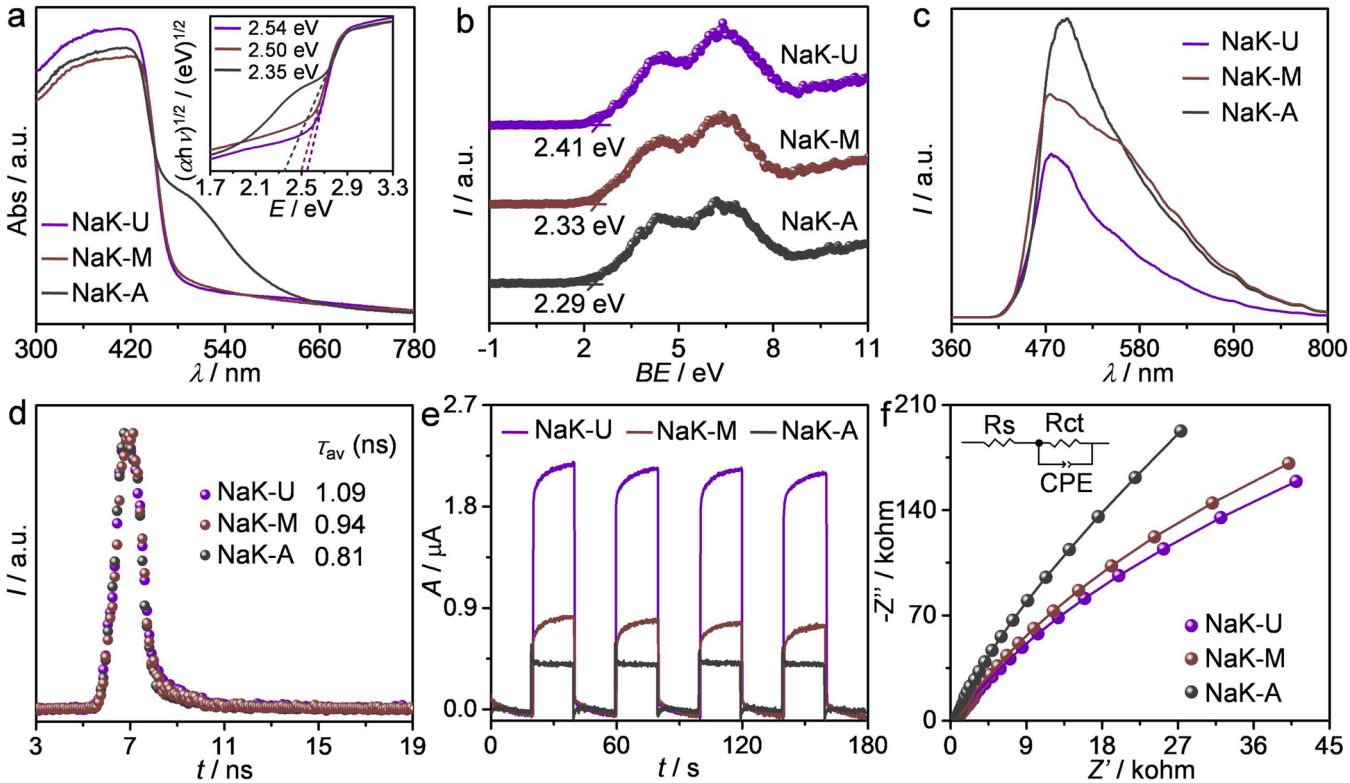

Fig. 4. The UV-vis DRS (a), corresponding Taut plots for the band gap energy (inset), VB-XPS spectra (b), room-temperature steady-state PL spectra (c), time-resolved photoluminescence decay (TRPD) spectra (d), transient photocurrent response (e), and EIS Nyquist plots (f) of NaK-U, NaK-M and NaK-A.

carriers were revealed by steady-state photoluminescence (PL) measurements and time-resolved transient PL decay (TRPD) spectra. As shown in Fig. 4c, significantly decreased PL emission intensity was observed for NaK-U in comparison with that of NaK-M and NaK-A, evidencing the improved charge separation efficiency, which could be ascribed to the built-in electrical field of the D-A heterojunctions and the reduced charge trapping sites caused by high crystallinity [60]. In addition, the TRPD spectra indicated a longer average lifetime of the charges for NaK-U (1.09 ns) in comparison with NaK-M (0.94 ns) and NaK-A (0.81 ns) (Fig. 4d), suggesting a higher possibility of the participation of the photogenerated carriers for the subsequent surface redox reactions in the case of NaK-U, which was beneficial for improving the catalytic performance in C−C bond cleavage.

The transient photocurrent response and electrochemical impedance spectroscopy (EIS) were also investigated to gain insight into the charge transport efficiency. Fig. 4e showed that all NaK-*X* samples exhibited steady and reproducible transient photocurrent responses under intermittently visible-light irradiation, among which NaK-U displayed field photocurrent response, followed by NaK-M and NaK-A. The results evidenced that the electron-hole separation and transfer efficiency were significantly enhanced in the order of NaK-U > NaK-M > NaK-A, consistent with the PL analysis. Moreover, among the tested photocatalysts, NaK-U with the smallest arc radius of the Nyquist cycle exhibited the lowest resistance for fast interfacial charge carrier transportation [61], characterized by EIS (Fig. 4f). Therefore, it could be concluded that the D-A heterojunction in NaK-U significantly facilitates the charge carriers dissociation and transfer by the synergetic interaction between triazine and heptazine units [62,63].

3.4. Mechanism investigation

To reveal the C−C bond cleavage mechanism of pp-ol over the NaK-U D-A heterojunctions under visible-light, control experiments with different substrates and active species trapping experiments were performed. As presented in Fig. 5a, reactions with benzaldehyde or phenyl formate showed negligible transformation under the optimized reaction condition (equations 1 −2), indicating that the C−C cleaved products are relatively stable during the photocatalytic process. In addition, pp-one was speculated as an intermediate resulting from the oxidation of pp-ol, affording 64.7 % conversion and 25.4 % yield of phenyl formate (equation 3). Considering that pp-one was almost negligible during the photocatalytic process, it indicates that the C−C bond cleavage was not carried out through the pp-one mediated reaction route. A control experiment under dark conditions showed negligible conversion as well as the aromatic monomers yield, manifesting the necessity of light irradiation (equation 4).

The active species trapping experiments were carried out in the presence of different scavengers to identify the active species that initiated the photocatalytic reaction. As shown in Fig. 5b, the presence of 2,2,6,6-tetramethyl-1-piperidinyloxy (TEMPO, radical scavenger), sodium thiosulfate ($K_2S_2O_4$, e^- scavenger) and ammonium oxalate ($(NH_4)_2C_2O_4$, h^+ scavenger) led to significant inhibition on the C−C bond cleavage, suggesting that the radical intermediates were more favorable for the reaction route, and the electrons and holes acted as the main active species that were responsible for the observed C−C bond cleavage over NaK-U. Noticeably, the addition of *p*-benzoquinone (*p*-BQ, $\bullet O_2^-$ scavenger) showed less inhibition effect on the pp-ol depolymerization. Besides, the •OH reactive species were excluded, since the addition of tert-butyl alcohol (*t*-BuOH, •OH radical scavenger) showed barely no influence on the photocatalytic performance. To be noted that a part of P1 or P2 products were further converted to benzoic acid or phenol, in the presence of $(NH_4)_2C_2O_4$ or *p*-BQ, respectively.

Furthermore, the ESR experiments were carried out for e^-–h^+ determination by using 2,2,6,6-tetramethylpiperidine-1-oxyl (TEMPO) as the trapping agent (Fig. 6a). As a typical spin label molecule, TEMPO containing unpaired electrons presented triplet ESR signals with an intensity ratio of 1:1:1 in the dark. With visible light irradiation, the signal intensity would be depressed due to the formation of TEMPOH and

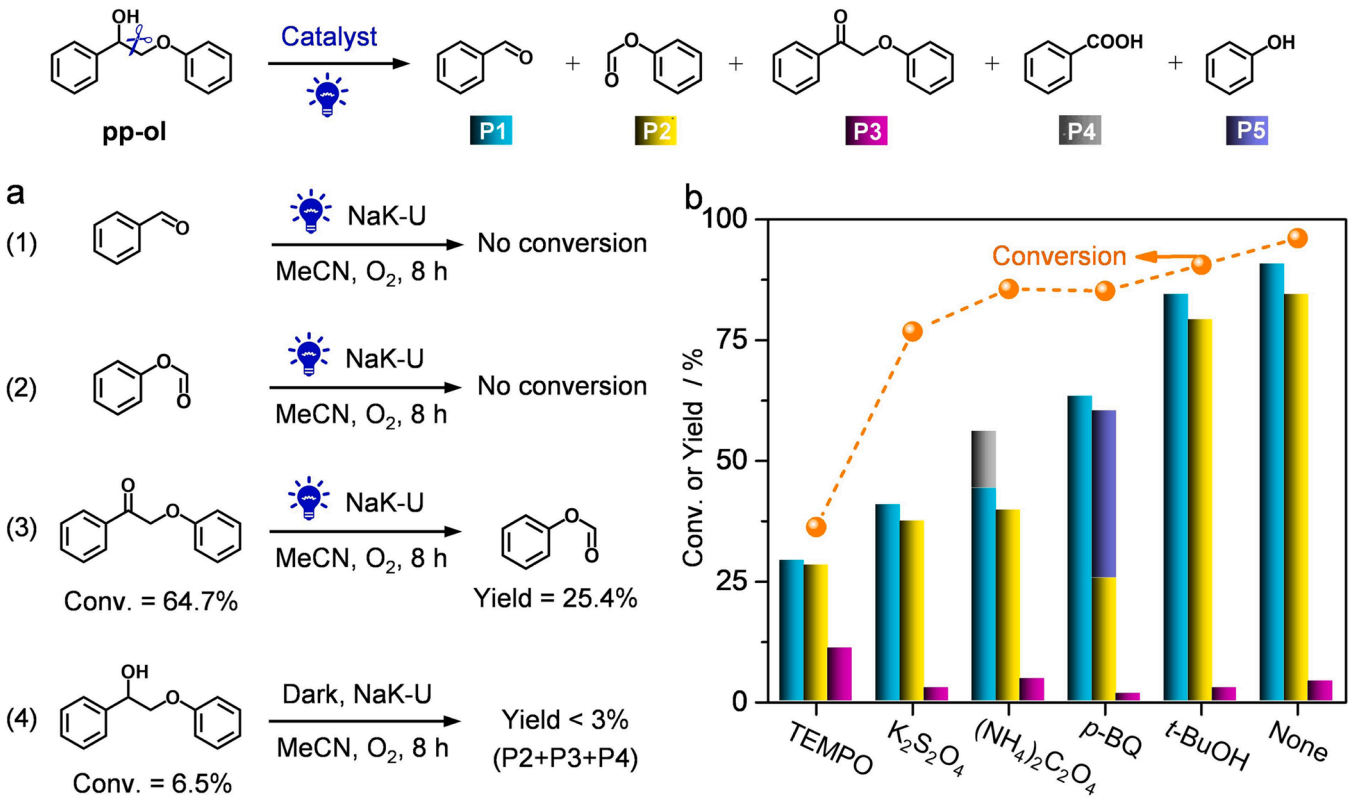

Fig. 5. Control experiments (a) and influence of different scavengers (b) on the photocatalytic activity of NaK-U in the C–C bond cleavage of pp-ol under visible-light.

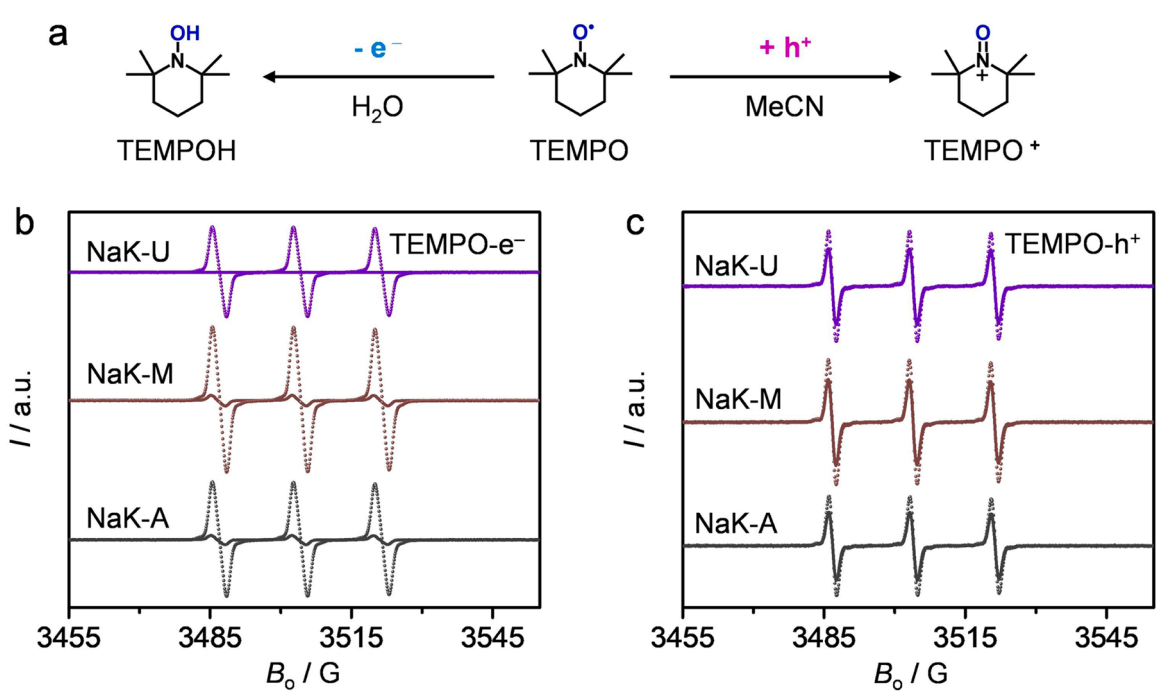

Fig. 6. Spin-trapping mechanism of TEMPO (a). TEMPO-trapping ESR spectra in aqueous dispersion for TEMPOH (b) and in MeCN dispersion for $TEMPO^+$ adduct (c). Dotted lines: dark; Solid lines: light.

$TEMPO^+$ adducts resulting from the TEMPO reacting with photo-generated e^- (in H_2O) or h^+ (in MeCN) [64]. As shown in Fig. 6b and c, TEMPO–e^- and TEMPO–h^+ displayed distinctly weakened characteristic peaks in the visible-light irradiation than that in the dark. This means that e^- and h^+ were significantly produced in NaK-*X* and captured by TEMPO under light irradiation, and further be employed acting as active species for C–C bond cleavage. Furthermore, the ESR response signals of TEMPO–e^- were significantly different, especially

disappearance in NaK-U, showing more photo-excited electrons on NaK-U as a consequence of D-A heterojunctions. The ESR results indicate that electron–hole separation and transfer efficiency of NaK-U were superior to NaK-M and NaK-A, which was consistent with the photo-electrochemical experiments.

To give more insight into the significant processes of charge transfer and electric field change, the surface photovoltage (SPV) spectra of PTI (triazine-based carbon nitride, T-CN), NaK-M (heptazine-based carbon nitride, H-CN), and NaK-U (triazine-heptazine-based carbon nitride, T/H-CN) have now been conducted (Fig. S7a). The intensity of the SPV signal is positively associated with the amount of photo-generated charge as well as the characteristics of spatial charge separation, and the sign (positive or negative) of photovoltage is correlated to the direction of the charges diffusion [65]. The negative SPV signals indicated that all carbon nitride samples are *n*-type semiconductors, which are expected to accumulate electrons on the photocatalyst surface, resulting in the reduction behavior of conduction bands. Notably, the T/H-CN exhibited an intensified SPV signal, demonstrating the superior charge transfer efficiency of the T/H-CN heterostructure to that of H-CN and T-CN.

According to Zhu's group [66] and the Eq. S3 (Supporting Information), the internal electric field IEF is mainly determined by the surface voltage (V_s)and zeta potential (ζ). Considering the ζ values of T-CN, T/H-CN, and T/H-CN are almost the same (Table S3), the E_{IEF} is mainly determined by V_s. As shown in Fig. S7b, the T/H-CN heterostructure exhibited an obviously stronger built-in electric field, which was 3.3 and 259 times higher than that of T-CN and T/H-CN, respectively. This giant interfacial electric field would significantly promote the efficient separation and transfer of interface charge. As a result of this directional charge separation, T/H-CN afforded an aromatic monomers production rate of 1.09 mmol g^{-1} h^{-1} as 2.2 and 10.9 times high as that of H-CN (0.49 mmol g^{-1} h^{-1}) and T-CN (0.1 mmol g^{-1} h^{-1}) respectively (Fig. S7c).

To better understand the contribution of the D-A heterojunctions on the observed photocatalytic activity enhancement, the electronic structures of the single-layer triazine, heptazine, and triazine-heptazine CN, which respectively correspond to the T-CN, H-CN, and T/H-CN heterojunction samples in experiments were calculated by using DFT calculations. The calculated highest occupied and lowest unoccupied states of the CN were displayed in Fig. 7. As for single-layer triazine and heptazine CN, the highest occupied and lowest unoccupied states were fully delocalized due to the high symmetry of planar structures. Noticeably, the highest occupied and lowest unoccupied states of the single-layer triazine-heptazine CN were localized on different structural units, indicating strong spatial separation of photo-generated electrons in the T/H-CN heterojunction resulting from the *in-situ* generated internal electric field. As a result, the constructed T/H-CN heterojunction gave rise to intramolecular charge transfer and migration, driving the electron from triazene (donor unit) to heptazine (acceptor unit). Furthermore, the adsorption energies (E_{ad}) of pp-ol were calculated on the surface of these structures (Fig. S8), showing the facilitated adsorption of pp-ol on T-CN with the smallest E_{ad} of − 1.35 eV, followed by H-CN (E_{ad} = −1.25 eV) and T/H-CN (E_{ad} = −0.90 eV). In addition, the distance (2.713 Å) between β-H atom in pp-ol molecule and the nitrogen atom in the single-layer T/H-CN is smaller than that of T-CN (3.120 Å) and H-CN (2.892 Å), meaning that the C_β−H bonds are more prone to break over T/H-CN and produce the crucial C_β radicals, which are pivotal for the substrate transformation and C−C bond cleavage process.

To investigate the photocatalytic process in more depth, we performed the ESR spin-trapping (5,5-dimethyl-1-pyrrolidinoxy-N-oxide (DMPO) serving as spin label molecule) and control experiments with deuterated lignin model substrates due to the absence of suitable hydrogen radical trapping agent. The formation of carbon radical species during the photocatalytic pp-ol depolymerization was validated by the ESR spectra with DMPO as a spin-label molecule [67]. Fig. S9 showed the ESR spectra obtained from DMPO-spin-trapping adduct before and during irradiation with simulated sunlight. The sextet ESR characteristic signals induced by the DMPO-carbon radical adduct were detected under the irradiation of a Xenon lamp, demonstrating the generation of carbon-centered radicals. Combined with the results of the active species trapping experiments (Fig. 5b), it is demonstrated that the photocatalytic process proceeds *via* a C-centered radical-mediated reaction mechanism and the C-centered radical is the key to the high activity and selectivity of C−C bond cleavage. To further clarify the C-centered radical origin, the isotopic experiments were performed under similar photocatalytic conditions by using the deuterated substrate at α-position (pp-ol') and β-position (pp-ol''). The deuterated benzaldehyde (P1') was observed (Fig. S10a), indicating that the C_α−D bond remained in the photocatalytic process. Furthermore, Fig. S10b demonstrated the formation of deuterated phenyl formate (P2') and deuterated pp-one (P3'') in the conversion of pp-ol''. This provides evidence for the formation of C_β-centered radical *via* the C_β−H bond cleavage triggered by the photogenerated holes, which releases proton H^+. As a result, hydrogen radical (H•) was formed by the reduction of H^+, and then participated in the subsequent reaction process (Fig. 8a).

Based on the aforementioned results, a possible mechanism of the photocatalytic C−C bond cleavage of pp-ol has been proposed for NaK-U (Fig. 8a). During the photocatalytic process, pp-ol molecular was first parallelly adsorbed on the NaK-U surface, which exhibited a large

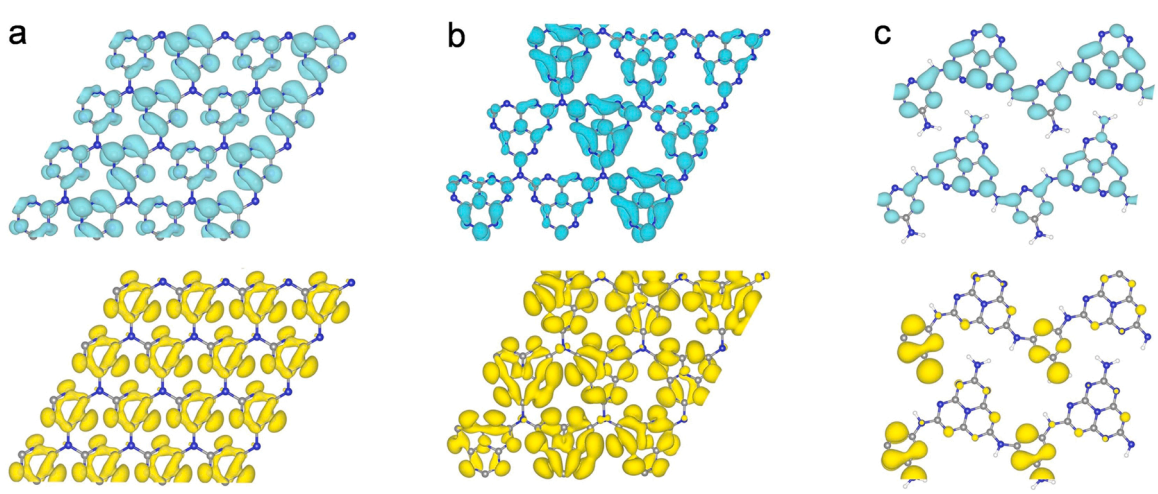

Fig. 7. Calculated highest occupied (yellow) and lowest unoccupied (cyan) states of the single-layer (a) triazine, (b) heptazine, and (c) triazine-heptazine g-C_3N_4. The isosurfaces were plotted at a value of 5×10^{-4} e/Å^3. N, blue; C, brown.

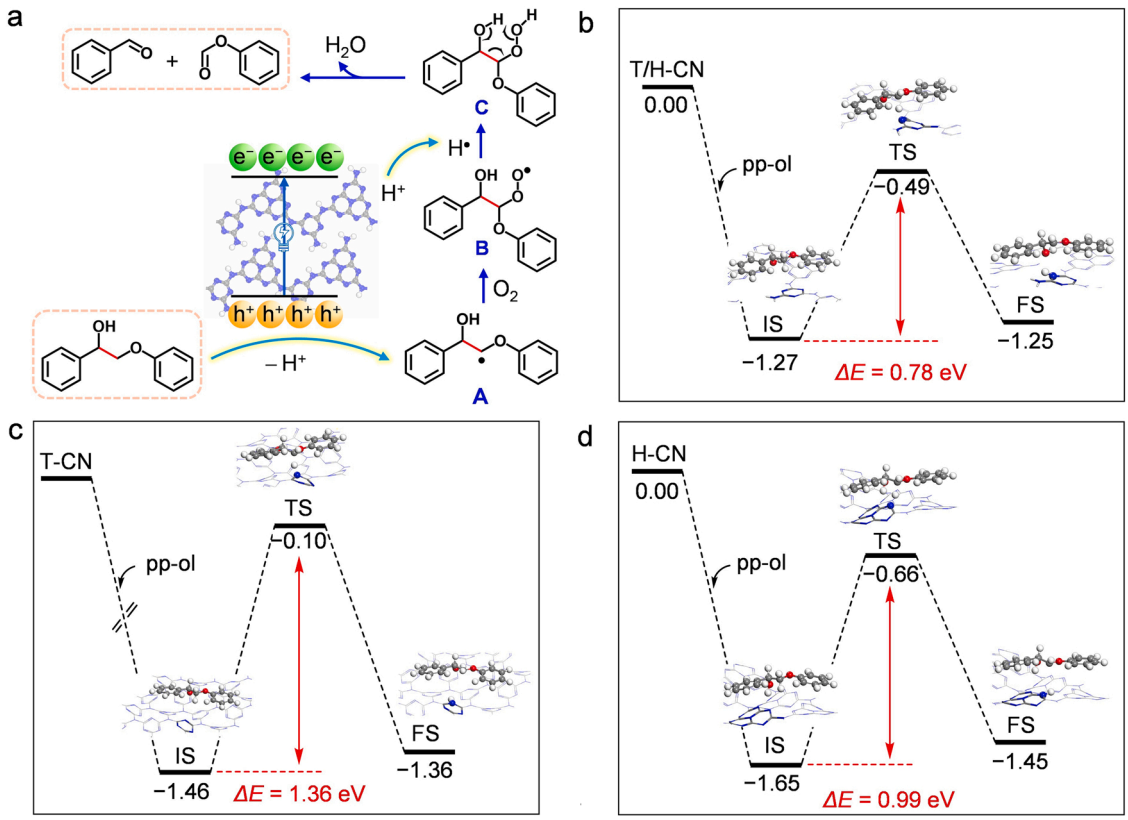

Fig. 8. (a) The proposed photocatalytic reaction mechanism of C−C bond cleavage of pp-ol over NaK-U under visible-light irradiation. Calculated energy profiles of pp-ol dehydrogenation on the single-layer (b) triazine-heptazine, (c) triazine, and (d) heptazine CN. IS, TS, and FS correspond to the initial, transition, and final states.

specific surface area for affording sufficient adsorption sites. Then, the H-atom abstraction occurred at C_β of pp-ol under the action of holes in VB, forming a C_β-centered radical (A), which resulted in the drastically decreased bond dissociation energy of the C═C bond. To analyze the propensity to the generation of radical A, the calculated potential energy diagrams for the photocatalytic dehydrogenation of pp-ol molecules on different carbon nitride surfaces and the geometry of various initial states (IS), transition states (TS), and final states (FS) were presented in Fig. 8b−d. The energy barrier of T/H-CN (0.78 eV) was significantly lower than that of T-CN (1.36 eV) and H-CN (0.99 eV) from an energetic standpoint, indicating an excellent dehydrogenation activity of T/H-CN. Subsequently, the C_β-centered radical A reacted with O_2 to afford radical B. Secondly, the electrons in the CB could reduce H^+ to produce H•, which further integrated with radical B to produce a peroxide intermediate (C). With the assistance of electron transfer in the six-membered ring transition state, the C−C bond in intermediate C is induced to cleavage, forming the major products of benzaldehyde and phenyl formate, accompanied by the left of an H_2O molecule. The as-described photocatalytic pathway is a redox process involving hole-coupled electron transfer.

4. Conclusion

In conclusion, we have successfully demonstrated the strategy of constructing triazine-heptazine D-A heterostructures for boosting the photocatalytic performance of the C−C bond cleavage of lignin models. Strikingly, almost 100 % conversion and high yields of aromatic compounds (up to 90.8 %) are achieved over triazine-heptazine-based carbon nitride heterojunctions for 2-phenoxy-1-phenylethanol under visible-light irradiation, exceeding the triazine- or heptazine-based counterparts. The integrated theoretic calculations and experimental results reveal that the significantly enhanced catalytic performance for the D-A heterostructure is due to the accelerated charge carriers separation and migration induced by the built-in electric field at the triazine-heptazine interface, and the facilitated substrate adsorption and C_β-radical generation. This work provides an efficient strategy for constructing intramolecular D-A heterostructures to optimize the charge-carriers separation and transport, which is instructive for photocatalytic selective cleavage of the lignin C−C linkages.

CRediT authorship contribution statement

Qingqing Zhang: Methodology, Investigation, Data curation, Formal analysis, Writing – Original Draft. **Yichun Chu:** DFT calculation, Formal analysis. **Zhulan Liu:** Resources. **Xin-Ping Wu:** DFT calculation, Writing – Review & Editing. **Xue-Qing Gong:** Writing – Review & Editing. **Zupeng Chen:** Conceptualization, Project administration, Writing – Review & Editing, Supervision, Funding acquisition.

Declaration of Competing Interest

The authors declare that they have no known competing financial interests or personal relationships that could have appeared to influence the work reported in this paper.

Data Availability

Data will be made available on request.

Acknowledgements

This work was supported by the National Natural Science Foundation of China (22202105), the Natural Science Foundation of Jiangsu Province (BK20210608) and the Natural Science Foundation of Jiangsu

Higher Education Institutions of China (21KJA150003).

Appendix A. Supporting information

Supplementary data associated with this article can be found in the online version at doi:10.1016/j.apcatb.2023.122688.

References

[1] X.J. Wu, N.C. Luo, S.J. Xie, H.K. Zhang, Q.H. Zhang, F. Wang, Y. Wang, Photocatalytic transformations of lignocellulosic biomass into chemicals, Chem. Soc. Rev. 49 (2020) 6198–6223, https://doi.org/10.1039/D0CS00314J.

[2] A.J. Ragauskas, G.T. Beckham, M.J. Biddy, R. Chandr, F. Chen, M.F. Davi, B. H. Davison, R.A. Dixon, P. Gilna, M. Keller, P. Langan, A.K. Naskar, J.N. Saddler, T. J. Tschaplinski, G.A. Tuskan, C.E. Wyman, Lignin valorization: improving lignin processing in the biorefinery, Science 344 (2014), 1246843, https://doi.org/10.1126/science.1246843.

[3] J.G. Zhang, Catalytic transfer hydrogenolysis as an efficient route in cleavage of lignin and model compounds, Green. Energy Environ. 3 (2018) 328–334, https://doi.org/10.1016/j.gee.2018.08.001.

[4] Z.H. Sun, G. Bottari, A. Afanasenko, M.C.A. Stuart, P.J. Deuss, B. Fridrich, K. Barta, Complete lignocellulose conversion with integrated catalyst recycling yielding valuable aromatics and fuels, Nat. Catal. 1 (2018) 82–92, https://doi.org/10.1038/s41929-017-0007-z.

[5] L. Dong, L.F. Lin, X. Han, X.Q. Si, X.H. Liu, Y. Guo, F. Lu, S. Rudić, S.F. Parker, S. H. Yang, Y.Q. Wang, Breaking the limit of lignin monomer production via cleavage of interunit carbon–carbon linkages, Chem 5 (2019) 1521–1536, https://doi.org/10.1016/j.chempr.2019.03.007.

[6] J. Zakzeski, P.C.A. Bruijnincx, A.L. Jongerius, B.M. Weckhuysen, The catalytic valorization of lignin for the production of renewable chemicals, Chem. Rev. 110 (2010) 3552–3599, https://doi.org/10.1021/cr900354u.

[7] R. Rinaldi, R. Jastrzebski, M.T. Clough, J. Ralph, M. Kennema, P.C.A. Bruijnincx, B. M. Weckhuysen, Paving the way for lignin valorisation: recent advances in bioengineering, biorefining and catalysis, Angew. Chem. - Int. Ed. 55 (2016) 8164–8215, https://doi.org/10.1002/anie.201510351.

[8] Q.Q. Zhang, N.K. Gupta, M. Rose, X.L. Gu, P.W. Menezes, Z.P. Chen, Mechanistic insights into the photocatalytic valorization of lignin models via C−O/C−C cleavage or C−C/C−N coupling 3 (2022) 1–57, https://doi.org/10.1016/j.checat.2022.11.009.

[9] Y.L. Wang, J.H. He, Y.T. Zhang, $CeCl_3$-promoted simultaneous photocatalytic cleavage and amination of C_α–C_β bond in lignin model compounds and native lignin, CCS Chem. 2 (2020) 107–117, https://doi.org/10.31635/ccschem.020.201900076.

[10] T.T. Hou, N.C. Luo, H.J. Li, M. Heggen, J.M. Lu, Y.H. Wang, F. Wang, Yin and yang dual characters of CuO_x clusters for C–C bond oxidation driven by visible light, ACS Catal. 7 (2017) 3850–3859, https://doi.org/10.1021/acscatal.7b00629.

[11] Y.L. Wang, Y. Liu, J.H. He, Y.T. Zhang, Redox-neutral photocatalytic strategy for selective C−C bond cleavage of lignin and lignin models via PCET process, Sci. Bull. 64 (2019) 1658–1666, https://doi.org/10.1016/j.scib.2019.09.003.

[12] S.T. Nguyen, P.R.D. Murray, R.R. Knowles, Light-driven depolymerization of native lignin enabled by proton-coupled electron transfer, ACS Catal. 10 (2020) 800–805, https://doi.org/10.1021/acscatal.9b04813.

[13] S. Gazi, M. Đokić, A.M.P. Moeljadi, R. Ganguly, H. Hirao, H.S. Soo, Kinetics and DFT studies of photoredox carbon–carbon bond cleavage reactions by molecular vanadium catalysts under ambient conditions, ACS Catal. 7 (2017) 4682–4691, https://doi.org/10.1021/acscatal.7b01036.

[14] H.F. Liu, H.J. Li, N.C. Luo, F. Wang, Visible-light-induced oxidative lignin C−C bond cleavage to aldehydes using vanadium catalysts, ACS Catal. 10 (2020) 632–643, https://doi.org/10.1021/acscatal.9b03768.

[15] Y.O. Wang, H. Suzuki, J.J. Xie, O. Tomita, D.J. Martin, M. Higashi, D. Kong, R. Abe, J.W. Tang, Mimicking natural photosynthesis: solar to renewable H_2 fuel synthesis by Z-scheme water splitting systems, Chem. Rev. 118 (2018) 5201–5241, https://doi.org/10.1021/acs.chemrev.7b00286.

[16] Y.T. Xiao, G.H. Tian, W. Li, Y. Xie, B.J. Jiang, C.G. Tian, D.Y. Zhao, H.G. Fu, Molecule self-assembly synthesis of porous few-layer carbon nitride for highly efficient photoredox catalysis, J. Am. Chem. Soc. 141 (2019) 2508–2515, https://doi.org/10.1021/jacs.8b12428.

[17] J.Y. Li, X.H. Wang, L. Huang, L. Tian, M. Shalom, C.Y. Xiong, H.J. Zhang, Q.L. Jia, S.W. Zhang, F. Liang, Ultrathin mesoporous graphitic carbon nitride nanosheets with functional cyano group decoration and nitrogen-vacancy defects for an efficient selective CO_2 photoreduction, Nanoscale 13 (2021) 12634–12641, https://doi.org/10.1039/D1NR02639A.

[18] M. Majdoub, Z. Anfar, A. Amedlous, Emerging chemical functionalization of g-C_3N_4: covalent/noncovalent modifications and applications, ACS Nano 14 (2020) 12390–12469, https://doi.org/10.1021/acsnano.0c06116.

[19] F. Li, M. Tang, T. Li, L.L. Zhang, C. Hu, Two-dimensional graphene/g-C_3N_4 in-plane hybrid heterostructure for enhanced photocatalytic activity with surface-adsorbed pollutants assistant, Appl. Catal. B-Environ. 268 (2020), 118397, https://doi.org/10.1016/j.apcatb.2019.118397.

[20] H.F. Liu, H.J. Li, J.M. Lu, S. Zeng, M. Wang, N.C. Luo, S.T. Xu, F. Wang, Photocatalytic cleavage of C–C bond in lignin models under visible light on mesoporous graphitic carbon nitride through π–π stacking interaction, ACS Catal. 8 (2018) 4761–4771, https://doi.org/10.1021/acscatal.8b00022.

[21] Y.Q. Wang, D.M. Zhao, H. Deng, M.T. Li, J. Chen, S.H. Shen, Theoretical insights into the limitation of photocatalytic overall water splitting performance of via group elements doped polymeric carbon nitride: a density functional theory calculation predicting solar-to-hydrogen efficiency, Sol. RRL 5 (2021), 2000630, https://doi.org/10.1002/solr.202000630.

[22] D.M. Zhao, C.L. Dong, B. Wang, C. Chen, Y.C. Huang, Z.D. Diao, S.Z. Li, L.J. Guo, S. H. Shen, Synergy of dopants and defects in graphitic carbon nitride with exceptionally modulated band structures for efficient photocatalytic oxygen evolution, Adv. Mater. 31 (2019), 1903545, https://doi.org/10.1002/adma.201903545.

[23] C.L. Zhu, T. Wei, Y. Wei, L. Wang, M. Lu, Y.P. Yuan, L.S. Yin, L. Huang, Unravelling intramolecular charge transfer in donor-acceptor structured g-C_3N_4 for superior photocatalytic hydrogen evolution, J. Mater. Chem. A 9 (2021) 1207–1212, https://doi.org/10.1039/d0ta08609f.

[24] X.Q. Fan, L.X. Zhang, R.L. Cheng, M. Wang, M.L. Li, Y.J. Zhou, J.L. Shi, Construction of graphitic C_3N_4-based intramolecular donor–acceptor conjugated copolymers for photocatalytic hydrogen evolution, ACS Catal. 5 (2015) 5008–5015, https://doi.org/10.1021/acscatal.5b01155.

[25] Y.R. Zheng, J. Dong, C.P. Huang, L.G. Xia, Q. Wu, Q.J. Xu, W.F. Yao, Co-doped Mo-Mo_2C cocatalyst for enhanced g-C_3N_4 photocatalytic H_2 evolution, Appl. Catal. B-Environ. 260 (2020), 118220, https://doi.org/10.1016/j.apcatb.2019.118220.

[26] J. Liu, H. Wang, M. Antonietti, Graphitic carbon nitride "reloaded": emerging applications beyond (photo)catalysis, Chem. Soc. Rev. 45 (2016) 2308–2326, https://doi.org/10.1039/c5cs00767d.

[27] H.J. Li, Y. Zhou, W.G. Tu, J.H. Ye, Z.G. Zou, State-of-the-art progress in diverse heterostructured photocatalysts toward promoting photocatalytic performance, Adv. Funct. Mater. 25 (2015) 998–1013, https://doi.org/10.1002/adfm.201401636.

[28] X.J. Wu, J.C. Lin, H.Z. Zhang, S.J. Xie, Q.H. Zhang, B.F. Sels, Ye Wang, Z-Scheme nanocomposite with high redox ability for efficient cleavage of lignin C−C bonds under simulated solar light, Green. Chem. 23 (2021) 10071–10078, https://doi.org/10.1039/d1gc03455c.

[29] G.G. Zhang, G.S. Li, T. Heil, S. Zafeiratos, F.L. Lai, A. Savateev, M. Antonietti, X. C. Wang, Tailoring the grain boundary chemistry of polymeric carbon nitride for enhanced solar hydrogen production and CO_2 reduction, Angew. Chem. - Int. Ed. 58 (2019) 3433–3437, https://doi.org/10.1002/anie.201811938.

[30] A. Notario-Estévez, S.M. Kozlov, F. Viñes, F. Illas, Electronic-structure-based chemical descriptors:(in) dependence on self-interaction and Hartree-Fock exchange, Phys. Rev. B 54 (1996) 11169–11186, https://doi.org/10.1039/C4CC10427G.

[31] G. Kresse, J. Furthmüller, Efficiency of ab-initio total energy calculations for metals and semiconductors using a plane-wave basis set, Comput. Mater. Sci. 6 (1996) 15–50, https://doi.org/10.1016/0927-0256(96)00008-0.

[32] J.P. Perdew, K. Burke, M. Ernzerhof, Generalized gradient approximation made simple, Phys. Rev. Lett. 77 (1996) 3865, https://doi.org/10.1103/PhysRevLett.77.3865.

[33] S. Grimme, Semiempirical GGA-type density functional constructed with a long-range dispersion correction, J. Comput. Chem. 27 (2006) 1787–1799, https://doi.org/10.1002/jcc.20495.

[34] P.E. Blöchl, Projector augmented-wave method, Phys. Rev. B 50 (1994) 17953, https://doi.org/10.1103/PhysRevB.50.17953.

[35] A. Savateev, S. Pronkin, J.D. Epping, M.G. Willinger, C. Wolff, D. Neher, M. Antonietti, D. Dontsova, Potassium poly(heptazine imides) from aminotetrazoles: shifting band gaps of carbon nitride-like materials for more efficient solar hydrogen and oxygen evolution, ChemCatChem 9 (2017) 167–174, https://doi.org/10.1002/cctc.201601165.

[36] Y.S. Xu, X. He, H. Zhong, D.J. Singh, L.J. Zhang, R.H. Wang, Solid salt confinement effect: an effective strategy to fabricate high crystalline polymer carbon nitride for enhanced photocatalytic hydrogen evolution, Appl. Catal. B-Environ. 246 (2019) 349–355, https://doi.org/10.1016/j.apcatb.2019.01.069.

[37] S.F. An, Y.K. Guo, X.Y. He, P. Gao, G.J. Hou, J.G. Hou, C.S. Song, X.W. Guo, Intermediate-induced repolymerization for constructing self-assembly architecture: Red crystalline carbon nitride nanosheets for notable hydrogen evolution, Appl. Catal. B-Environ. 310 (2022), 121323, https://doi.org/10.1016/j.apcatb.2022.121323.

[38] Z.Z. Sun, H.Z. Dong, Q. Yuan, Y.Y. Tan, W. Wang, Y.B. Jiang, J.Y. Wan, J.W. Wen, J.J. Yang, J.Q. He, T. Cheng, L.M. Huang, Self-supported hierarchical crystalline carbon nitride arrays with triazine-heptazine heterojunctions for highly efficient photoredox catalysis, Chem. Eng. J. 435 (2022), 134865, https://doi.org/10.1016/j.cej.2022.134865.

[39] H.H. Liu, D.L. Chen, Z.Q. Wang, H.J. Jing, R. Zhang, Microwave-assisted molten-salt rapid synthesis of isotype triazine-/heptazine based g-C_3N_4 heterojunctions with highly enhanced photocatalytic hydrogen evolution performance, Appl. Catal. B-Environ. 203 (2017) 300–313, https://doi.org/10.1016/j.apcatb.2016.10.014.

[40] A.L. Jin, X. Liu, M.R. Li, Y.S. Jia, C.F. Chen, X.S. Chen, One-pot ionothermal synthesized carbon nitride heterojunction nanorods for simultaneous photocatalytic reduction and oxidation reactions: synergistic effect and mechanism insight, ACS Sustain. Chem. Eng. 7 (2019) 5122–5133, https://doi.org/10.1021/acssuschemeng.8b05969.

[41] Y. Li, F. Gong, Q. Zhou, X.H. Feng, J.J. Fan, Q.J. Xiang, Crystalline isotype heptazine-/triazine-based carbon nitride heterojunctions for an improved hydrogen evolution, Appl. Catal. B-Environ. 268 (2020), 118381, https://doi.org/10.1016/j.apcatb.2019.118381.

[42] G.G. Zhang, L.H. Lin, G.S. Li, Y.F. Zhang, A. Savateev, S. Zafeiratos, X.C. Wang, M. Antonietti, Ionothermal synthesis of triazine-heptazine-based copolymers with apparent quantum yields of 60% at 420 nm for solar hydrogen production from

"sea water", Angew. Chem. -Int. Ed. 130 (2018) 9516–9520, https://doi.org/10.1002/anie.201804702.
[43] I. Krivtsov, D. Mitoraj, C. Adler, M. Ilkaeva, M. Sardo, L. Mafra, C. Neumann, A. Turchanin, C.Y. Li, B. Dietzek, R. Leiter, J. Biskupek, U. Kaiser, C. Im, B. Kirchhoff, T. Jacob, R. Beranek, Water-soluble polymeric carbon nitride colloidal nanoparticles for highly selective quasi-homogeneous photocatalysis, Angew. Chem. -Int. Ed. 59 (2020) 487–495, https://doi.org/10.1002/anie.201913331.
[44] L. Luo, Z.Y. Gong, J.N. Ma, K.R. Wang, H.X. Zhu, K.Y. Li, L.Q. Xiong, X.W. Guo, J. W. Tang, Ultrathin sulfur-doped holey carbon nitride nanosheets with superior photocatalytic hydrogen production from water, Appl. Catal. B-Environ. 284 (2021), 119742, https://doi.org/10.1016/j.apcatb.2020.119742.
[45] Z.P. Chen, E. Vorobyeva, S. Mitchell, E. Fako, N. López, S.M. Collins, R.K. Leary, P. A. Midgley, R. Hauer, J. Pérez-Ramírez, Single-atom heterogeneous catalysts based on distinct carbon nitride scaffolds, Natl. Sci. Rev. 5 (2018) 642–652, https://doi.org/10.1093/nsr/nwy048.
[46] T.Y. Ma, S. Dai, M. Jaroniec, S.Z. Qiao, Graphitic carbon nitride nanosheet-carbon nanotube three-dimensional porous composites as high-performance oxygen evolution electrocatalysts, Angew. Chem. - Int. Ed. 53 (2014) 7281–7285, https://doi.org/10.1016/10.1002/anie.201403946.
[47] G.Q. Zhang, Y.S. Xu, M. Rauf, J.Y. Zhu, Y.L. Li, C.X. He, X.Z. Ren, P.X. Zhang, H. W. Mi, Breaking the limitation of elevated coulomb interaction in crystalline carbon nitride for visible and near-infrared light photoactivity, Adv. Sci. 9 (2022), 2201677, https://doi.org/10.1002/advs.202201677.
[48] Hj Yu, R. Shi, Y.X. Zhao, T. Bian, Y.F. Zhao, C. Zhou, G.I.N. Waterhouse, L.Z. Wu, C. H. Tung, T.R. Zhang, Alkali-assisted synthesis of nitrogen deficient graphitic carbon nitride with tunable band structures for efficient visible-light-driven hydrogen evolution, Adv. Mater. 29 (2017), 1605148, https://doi.org/10.1002/adma.201605148.
[49] W. Ren, J.J. Cheng, H.H. Ou, C.J. Huang, M. Anpo, X.C. Wang, Optimizing the crystallization process of conjugated polymer photocatalysts to promote electron transfer and molecular oxygen activation, J. Catal. 389 (2020) 636–645, https://doi.org/10.1016/j.jcat.2020.07.005.
[50] Y.S. Xu, X. He, H. Zhong, D.J. Singh, L.J. Zhang, R.H. Wang, Solid salt confinement effect: an effective strategy to fabricate high crystalline polymer carbon nitride for enhanced photocatalytic hydrogen evolution, Appl. Catal. B-Environ. 246 (2019) 349–355, https://doi.org/10.1016/j.apcatb.2019.01.069.
[51] G.Q. Zhang, Y.S. Xu, D.F. Yan, C.X. He, Y.L. Li, X.Z. Ren, P.X. Zhang, H.W. Mi, Construction of K^+ ion gradient in crystalline carbon nitride to accelerate exciton dissociation and charge separation for visible light H_2 production, ACS Catal. 11 (2021) 6995–7005, https://doi.org/10.1021/acscatal.1c00739.
[52] K. Li, W.D. Zhang, Creating graphitic carbon nitride based donor-π–acceptor-π–donor structured catalysts for highly photocatalytic hydrogen evolution, Small 14 (2018), 1703599, https://doi.org/10.1002/smll.201703599.
[53] X.Y. Wang, J.Q. Meng, X.Y. Zhang, Y.Q. Liu, M. Ren, Y.Y. Yang, Y.H. Guo, Controllable approach to carbon-deficient and oxygen-doped graphitic carbon nitride: Robust photocatalyst against recalcitrant organic pollutants and the mechanism insight, Adv. Funct. Mater. 31 (2021), 2010763, https://doi.org/10.1002/adfm.202010763.
[54] F.S. Guo, B. Hu, C. Yang, J.H. Zhang, Y.D. Hou, X.C. Wang, On-surface polymerization of in-plane highly ordered carbon nitride nanosheets toward photocatalytic mineralization of mercaptan gas, Adv. Mater. 33 (2021), 2101466, https://doi.org/10.1002/adma.202101466.
[55] G.G. Liu, G.X. Zhao, W. Zhou, Y.Y. Liu, H. Pang, H.B. Zhang, D. Hao, X.G. Meng, P. Li, T. Kako, J.H. Ye, In situ bond modulation of graphitic carbon nitride to construct p–n homojunctions for enhanced photocatalytic hydrogen production, Adv. Funct. Mater. 26 (2016) 6822–6829, https://doi.org/10.1002/10.1002/adfm.201602779.
[56] J. Zhang, X.C. Liang, C. Zhang, L.H. Lin, W.D. Xing, Z.Y. Yu, G.G. Zhang, X. C. Wang, Improved charge separation in poly(heptazine-triazine) imides with semi-coherent interfaces for photocatalytic hydrogen evolution, Angew. Chem. - Int. Ed. 61 (2022), e202210849, https://doi.org/10.1002/anie.202210849.
[57] G.G. Zhang, A. Savateev, Y.B. Zhao, L.N. Li, M. Antonietti, Advancing the n→π^* electron transition of carbon nitride nanotubes for H_2 photosynthesis, J. Mater. Chem. A 5 (2017) 12723–12728, https://doi.org/10.1039/c7ta03777e.
[58] C. Wan, L. Zhou, L. Sun, L.X. Xu, D.G. Cheng, F.Q. Chen, X.L. Zhan, Y.R. Yang, Boosting visible-light-driven hydrogen evolution from formic acid over AgPd/2D g-C_3N_4 nanosheets Mott-Schottky photocatalyst, Chem. Eng. J. 396 (2020), 125229, https://doi.org/10.1016/j.cej.2020.125229.
[59] C.M. Li, H.H. Wu, D.Q. Zhu, T.X. Zhou, M. Yan, G. Chen, J.X. Sun, G. Dai, F. Ge, H. J. Hong, High-efficient charge separation driven directionally by pyridine rings grafted on carbon nitride edge for boosting photocatalytic hydrogen evolution, Appl. Catal. B-Environ. 297 (2021), 120433, https://doi.org/10.1016/j.apcatb.2021.120433.
[60] Z.X. Zeng, H.T. Yu, X. Quan, S. Chen, S.S. Zhang, Structuring phase junction between tri-s-triazine and triazine crystalline C_3N_4 for efficient photocatalytic hydrogen evolution, Appl. Catal. B-Environ. 227 (2018) 153–160, https://doi.org/10.1016/j.apcatb.2018.01.023.
[61] M. Ren, X.Y. Zhang, Y.Q. Liu, G. Yang, L. Qin, J.Q. Meng, Y.H. Guo, Y.X. Yang, Interlayer palladium-single-atom-coordinated cyano-group-rich graphitic carbon nitride for enhanced photocatalytic hydrogen production performance, ACS Catal. 12 (2022) 5077–5093, https://doi.org/10.1021/acscatal.2c00427.
[62] Z. Yu, X. Yue, J. Fan, Q.J. Xiang, Crystalline intramolecular ternary carbon nitride homojunction for photocatalytic hydrogen evolution, ACS Catal. 12 (2022) 6345–6358, https://doi.org/10.1021/acscatal.2c01563.
[63] F. Li, T. Li, L.L. Zhang, Y. Jin, C. Hu, Enhancing photocatalytic performance by direct photo-excited electron transfer from organic pollutants to low-polymerized graphitic carbon nitride with more C-NH/NH_2 exposure, Appl. Catal. B-Environ. 296 (2021), 120316, https://doi.org/10.1016/j.apcatb.2021.120316.
[64] M.S. Li, L.X. Zhong, W. Chen, Y.M. Huang, Z.X. Chen, D.Q. Xiao, R. Zou, L. Chen, Q. Hao, Z.H. Liu, R.C. Sun, X.W. Peng, Regulating the electron–hole separation to promote selective oxidation of biomass using ZnS@Bi_2S_3 nanosheet catalyst, Appl. Catal. B-Environ. 292 (2021), 120180, https://doi.org/10.1016/j.apcatb.2021.120180.
[65] Y.B. Zhao, P. Zhang, Z.C. Yang, L.N. Li, J.Y. Gao, S. Chen, T.F. Xie, C.Z. Diao, S. B. Xi, B.B. Xiao, C. Hu, W. Choi, Mechanistic analysis of multiple processes controlling solar-driven H_2O_2 synthesis using engineered polymeric carbon nitride, Nat. Commun. 12 (2021) 3701, https://doi.org/10.1038/s41467-021-24048-1.
[66] Z.J. Zhang, X.J. Chen, H.J. Zhang, W.X. Liu, W. Zhu, Y.F. Zhu, A highly crystalline perylene imide polymer with the robust built-in electric field for efficient photocatalytic water oxidation, Adv. Mater. 32 (2020), 1907746, https://doi.org/10.1002/adma.201907746.
[67] H. Yoo, M.W. Lee, S. Lee, J. Lee, S. Cho, H. Lee, H.G. Cha, H.S. Kim, Enhancing photocatalytic β-O-4 bond cleavage in lignin model compounds by silver-exchanged cadmium sulfide, ACS Catal. 10 (2020) 8465–8475, https://doi.org/10.1021/acscatal.0c01915.